

## Research Article

# Dynamic Mechanical Characteristics and Constitutive Modeling of Rail Steel over a Wide Range of Temperatures and Strain Rates

Peijie Liu , Yanming Quan , and Guo Ding 

*School of Mechanical and Automotive Engineering, South China University of Technology, Guangzhou 510640, China*

Correspondence should be addressed to Yanming Quan; [meymquan@scut.edu.cn](mailto:meymquan@scut.edu.cn)

Received 12 December 2018; Revised 17 January 2019; Accepted 4 February 2019; Published 6 March 2019

Academic Editor: Paolo Ferro

Copyright © 2019 Peijie Liu et al. This is an open access article distributed under the Creative Commons Attribution License, which permits unrestricted use, distribution, and reproduction in any medium, provided the original work is properly cited.

Rail steel plays an indispensable role in the safety and stability of the railway system. Therefore, a suitable constitutive model is quite significant to understand the mechanical behavior of this material. Here, the compressive mechanical behavior of heat-treated U71Mn rail steel over a wide range of strain rates ( $0.001\text{ s}^{-1}$ – $10000\text{ s}^{-1}$ ) and temperatures ( $20^{\circ}\text{C}$ – $800^{\circ}\text{C}$ ) was systematically investigated via uniaxial quasistatic and dynamic tests. The split Hopkinson pressure bar (SHPB) apparatus was utilized to perform dynamic mechanical tests. The effects of temperature, strain, and strain rate on the dynamic compressive characteristics of U71Mn were discussed, respectively. The results indicate that the flow response of U71Mn is both temperature-sensitive and strain rate-sensitive. However, the influence of temperature on the flow response is more remarkable than that of strain rate. On the basis of the experimental data, the original and modified Johnson–Cook (JC) models of the studied material were established, respectively. Using correlation coefficient and average absolute relative error parameters, it is revealed that better agreement between the experimental and predicted stress is reached by the modified JC model, which demonstrates that the modified one can characterize the mechanical behavior of the studied material preferably.

## 1. Introduction

Rail steel is one of the most significant infrastructures in the railway network, which plays an indispensable role in the security and stability of the railway system. With the fast expansion of railway transportation around the world, rail steel in service is subjected to complex and dynamic loading imposed by railway wheels, which easily generates rail defects involving corrugation, squats, spalling, cracks, and so on [1–4]. Grassie [5] conducted an in-depth review on the development of rail corrugation and deepened its understanding. Zhong et al. [6] studied the rail crack growth with respect to rolling contact fatigue via the analysis of the chemical constituents and mechanical properties. Steenbergen and Dollevoet [7] studied the physical characteristics of rail squat initiation by a phenomenological analysis. Steenbergen [8] carried out an experimental investigation on the rail grinding-related rolling contact fatigue and analyzed the characteristics of rail spalling defects. These aforementioned undesirable defects severely

influence the safety of railway transportation if they are not effectively dealt with. Therefore, it has become increasingly significant to reprofile rails to remove defects in time. The dynamic flow response of materials is connected with temperature and strain rate, along with strain [9]; hence, an appropriate constitutive model to understand the flow behavior of rail steel is requested. For the sake of characterizing the stress-strain behavior under dynamic deformation conditions, the well-established split Hopkinson pressure bar (SHPB) technique which was initially designed by Kolsky is one of the most widely utilized testing means [10].

In recent years, some empirical (e.g., Johnson–Cook model), semiempirical (e.g., Zerilli–Armstrong model), and physically-based (e.g., Mechanical Threshold Stress model) constitutive equations have been put forward to characterize the flow response of materials [11–13]. Zerilli and Armstrong [12] put forward the Zerilli–Armstrong (ZA) model on the basis of dislocation mechanics. The Mechanical Threshold Stress (MTS) model put forward by Follansbee and Kocks [13]

is one of the physically-based models, and these kinds of models are not always preferred for the reason that more data obtained from accurately manipulated experimental conditions are required. More importantly, there are more material constants encompassed in semiempirical and physically-based models whose material constants are more difficult to derive than the empirical ones. The Johnson–Cook (JC) model [11] is an empirically-based model and it is extensively utilized to express the mechanical behavior of materials at large strain rates and high temperatures. Thanks to the advantages of simple expression, low computational complexity, and fast calculation speed, the JC model has gained widespread implementation in a diversity of finite element analysis software [14]. Nevertheless, the JC constitutive model in its original form is often unable to guarantee enough accuracy on the flow stress prediction of materials. Therefore, it is a necessity to modify the conventional JC model to express the flow response with sufficient prediction precision over a wide range of temperatures and strain rates. Gambirasio and Rizzi [15] put forward the split JC model which demonstrated that the capacity of the model to characterize the mechanical response of the studied material was conspicuously enhanced. Wang et al. [16] conducted a research on the dynamic deformation behavior of Inconel 718 under large strain rates and elevated temperatures, and they established a modified JC model with adequate accuracy. Zhao et al. [17] performed a research on the original and modified JC models to describe the mechanical behavior of the FeCr alloy acquired by laser additive manufacturing under wide strain rates and temperature ranges and found that the modified JC model could generate precise prediction of the mechanical behavior of the studied material.

Currently, although comparatively more existing researches emphasizing the deformation mechanism under large strain rate situations [18, 19], high-temperature deformation [20], and dynamic fracture [21] of other steels and alloys are available, there are very few systematic researches available that address the dynamic mechanical response of rail materials over a wide range of strain rates and temperatures (especially under large strain rates and high temperatures). Nakkalil et al. [22] performed a research focused on the mechanical response of rail steels under large strain rates and elevated temperatures, but no constitutive model was established in the article. Jing et al. [23] investigated the mechanical performance of train wheel materials under large strain rates via the split Hopkinson tensile bar (SHTB) equipment, and their research demonstrated that the tensile properties of the materials relied on strain rate.

In this study, the dynamic mechanical characteristics of heat-treated U71Mn rail steel are systematically investigated over a wide range of strain rates ( $0.001\text{ s}^{-1}$ – $10000\text{ s}^{-1}$ ) and temperatures ( $20^{\circ}\text{C}$ – $800^{\circ}\text{C}$ ) by virtue of the split Hopkinson pressure bar equipment. Based on the results of mechanical tests, the effects of strain rate and temperature along with strain on the flow stress of U71Mn rail steel are assessed. Furthermore, the strain rate sensitivity, temperature sensitivity, and strain hardening effect of the studied material are also discussed, respectively. Finally, the original and

modified JC models are established on the basis of the experimental data, respectively. In contrast, it is verified that the modified JC model can represent the flow response of the studied material more accurately by means of correlation coefficient ( $R$ ) and average absolute relative error (AARE).

## 2. Materials and Methods

**2.1. Materials.** The typical structure of a flat bottom rail comprises rail head, rail web, and rail foot, as shown in Figure 1. Compared with the rail web and rail foot, the rail head has a higher strength requirement to interact safely with railway wheels. The tested rail specimens were sampled from the heat-treated Mn-steel rail (Chinese brand: U71Mn) which is made from high carbon steel to provide high fatigue toughness. After the hot rolling process of U71Mn rail steel by the universal mill, the surplus heat of the rail head was  $850^{\circ}\text{C}$ , and the afterheat generated after the hot rolling process was further used to online slack-quench the rail via compressed air cooling technique performed in the rail manufacturer, during which the air cooling rate was set to  $3^{\circ}\text{C/s}$ . When the temperature of the rail head was  $500^{\circ}\text{C}$ , the rail was then air cooled to room temperature with the cooling rate of  $0.1^{\circ}\text{C/s}$ . The purpose of the rail heat-treatment is to acquire the final expected mechanical properties to extend the rail service life. U71Mn rails ( $60\text{ kg/m}$ ) are extensively employed in current Chinese high-speed railway network [24]. Tables 1 and 2 give the detailed chemical compositions and physical properties of the material, respectively. After the process of fine grinding, polishing, and etching, the typical microstructure of U71Mn rail steel is shown in Figure 2 under a scanning electron microscope (SEM, Quanta 200, FEI). The tested material displays a fully pearlitic microstructure with equiaxed pearlite colonies.

The tested rail material was in unused condition (never in service). All of the specimens for the purpose of mechanical testing were sampled from the rail head by electric discharge machining (EDM), and the sampling positions are shown in Figure 3. For the quasistatic compressive and dynamic compressive tests, all of the tested specimens were cylindrical in shape: the specimens used in the former test had a size of  $\Phi 8\text{ mm} \times 12\text{ mm}$ , and the specimens used in the latter test had a size of  $\Phi 5\text{ mm} \times 5\text{ mm}$  (for the test at the strain rate of  $1500\text{ s}^{-1}$ ) and  $\Phi 2\text{ mm} \times 2\text{ mm}$  (for the test at  $5000\text{ s}^{-1}$  and  $10000\text{ s}^{-1}$ ). Due to the same slenderness ratio of samples under dynamic loading conditions, the geometry effect of the specimens on the experimental results can be neglected. For every test condition, each group of the specimens was repeatedly conducted 6 times so as to ensure the reproducibility, and the averaged data under each test condition were adopted as the final experimental results.

**2.2. Experimental Procedure.** Uniaxial quasistatic compressive tests were performed via a Gleeble 3500 thermal simulation machine at  $0.001\text{ s}^{-1}$  and room temperature  $20^{\circ}\text{C}$ . The Gleeble 3500 device is a thermal and mechanical testing machine with wholly integrated digital closed-loop control. Each end face of the samples was properly

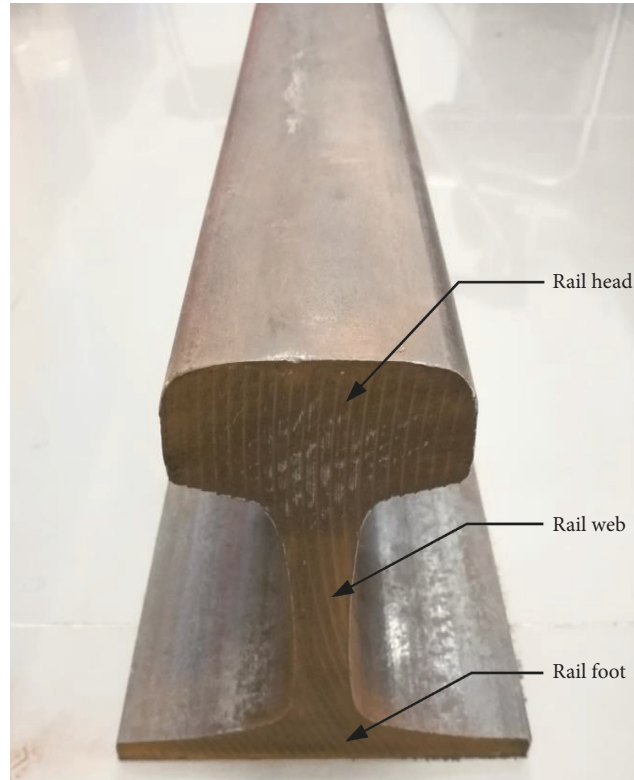


FIGURE 1: Typical structure of a flat bottom rail track.

TABLE 1: Chemical constituents (wt.%) of U71Mn.

| Material | C         | Mn        | Si        | S      | P     | Fe      |
|----------|-----------|-----------|-----------|--------|-------|---------|
| U71Mn    | 0.65–0.76 | 0.70–1.20 | 0.15–0.58 | ≤0.025 | ≤0.03 | Balance |

TABLE 2: Physical properties of U71Mn.

| Mechanical properties        | Values | Thermal properties              | Values |
|------------------------------|--------|---------------------------------|--------|
| Density (kg/m <sup>3</sup> ) | 7800   | Thermal conductivity (W/(m·°C)) | 51     |
| Young's modulus (GPa)        | 210    | Specific heat (J/(kg·°C))       | 500    |
| Poisson's ratio              | 0.3    | Melting point (°C)              | 1469   |

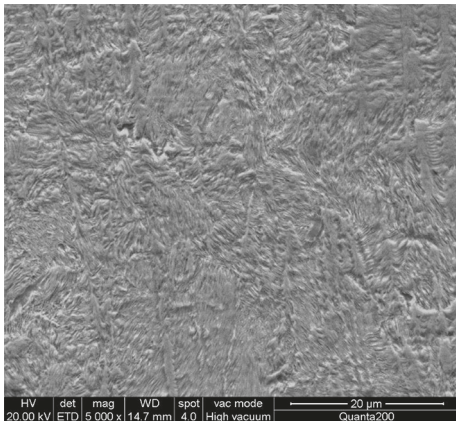


FIGURE 2: SEM graph of heat-treated U71Mn rail steel.

lubricated to diminish the undesirable friction effect before the test.

The SHPB technique has been extensively accepted to measure the stress-strain behavior from  $10^2 \text{ s}^{-1}$  to  $10^4 \text{ s}^{-1}$  [25]. According to [26], the SHPB technique serves as an accurate method which makes the experimenter induce various stress histories within the cylindrical samples. A split Hopkinson pressure bar (SHPB) apparatus with a synchronously assembled heating system was utilized to perform dynamic compressive tests, as shown in Figure 4(a). This apparatus enables to keep the sample at the center of the furnace while keeping the incident and transmitted bars outside the heating range of the furnace whose temperature is controlled by a PID closed-loop controller. In other words, when the sample with cylindrical shape is heated by the separate resistance furnace, the incident and transmitted bars are kept away from the heating zone of the furnace. Figure 4(b) displays the detailed configuration of the sample fixed during the high-temperature dynamic test, a K-type thermocouple attached to the sample is used to measure the sample temperature. The thermocouple itself is supported by a sleeve (namely, a thin tube) which can move freely along the axial direction of the bars. The thermocouple also plays a role in maintaining the specimen at the appropriate position inside the furnace before dynamic loading. When the temperature of the sample initially reaches the required value, the sample is maintained at the constant temperature for 2 minutes to ensure the homogeneous temperature distribution within the specimen, and then the bars are brought into contact with the specimen through the bar mover immediately before the stress pulse

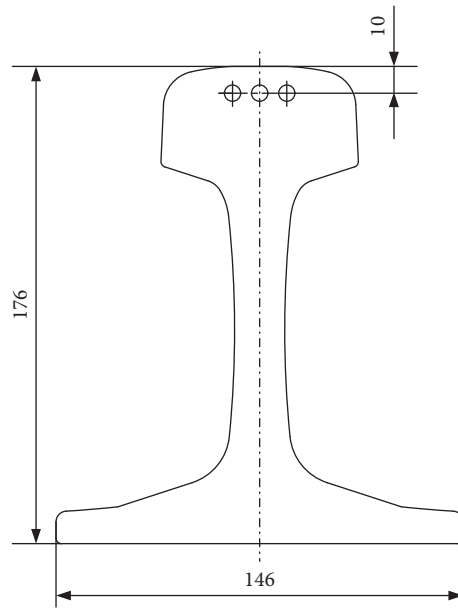


FIGURE 3: Sampling positions of the tested specimens.

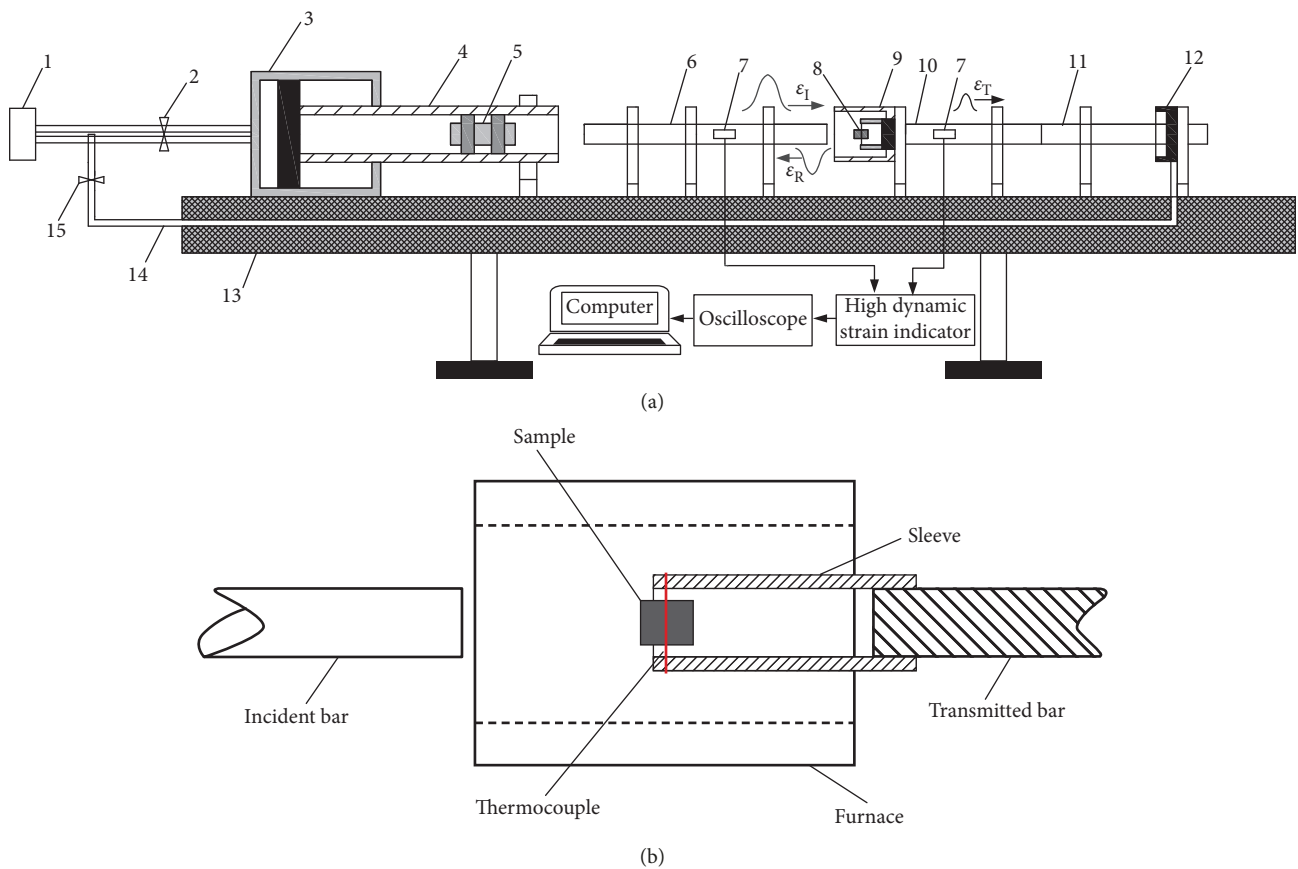


FIGURE 4: Experimental setup for dynamic tests. (a) Schematic of the SHPB equipment with a synchronously assembled heating system ( $\epsilon_i$ ,  $\epsilon_R$ , and  $\epsilon_T$  refer to strain signals from incident waves, reflected waves, and transmitted waves, respectively). 1, nitrogen gas gun; 2, inlet valve; 3, air chamber; 4, barrel; 5, striker bar; 6, incident bar; 7, strain gauge; 8, specimen; 9, heating furnace; 10, transmitted bar; 11, energy absorption bar; 12, bar mover; 13, support; 14, air pipe; 15, magnetic outlet valve. (b) Detailed configuration of the sample fixed during the high-temperature dynamic test.

arrives at the end of the incident bar. The bar mover is driven by the same gas gun which propels the striker bar towards the incident bar. To diminish the friction effect, the contact regions between the sample and the bars are properly lubricated with a grease containing molybdenum (Mo). When the incident bar is struck by the ultrahigh-strength steel striker bar driven by a pressurized nitrogen gas gun, a compressively longitudinal wave is created and transmitted down the incident bar. As the incident pulse arrives at the sample-bars interfaces, it partly returns to the incident bar whilst the remaining pulse is introduced into the transmitted bar on account of the mechanical impedance mismatch between the pressure bars and the sample. Strain gauges fixed onto the incident bar are employed to acquire the incident and reflected pulses, and strain gauges glued onto the transmitted bar are utilized to measure the transmitted pulse. These three strain pulses are recorded by an oscilloscope.

On the basis of the theory of one-dimensional wave propagation, the stress  $\sigma(t)$ , strain  $\varepsilon(t)$ , and strain rate  $\dot{\varepsilon}(t)$  of the specimen are expressed as

$$\begin{aligned}\sigma(t) &= \frac{A_0}{A_s} E \varepsilon_T, \\ \varepsilon(t) &= -\frac{2c_0}{l_s} \int_0^t \varepsilon_R dt, \\ \dot{\varepsilon}(t) &= -\frac{2c_0}{l_s} \dot{\varepsilon}_R,\end{aligned}\quad (1)$$

where  $A_0$  represents the cross-sectional area of the bars;  $E$  denotes Young's modulus of the bars;  $c_0$  ( $c_0 = \sqrt{E/\rho}$ , where  $\rho$  is the density of the pressure bars) represents the propagation velocity of one-dimensional elastic longitudinal wave;  $A_s$  means the initial cross-section area of the specimen;  $l_s$  refers to the specimen length; and  $\varepsilon_T$  and  $\varepsilon_R$  represent the strain signals of the transmitted and reflected wave, respectively.

### 3. Results and Discussion

Figure 5 shows the quasistatic compressive stress-strain curve of U71Mn rail steel at  $0.001 \text{ s}^{-1}$  and  $20^\circ\text{C}$ . It can be observed that the tested material undergoes remarkable strain hardening with the increasing plastic strain.

In order to verify the stress-state equilibrium at both end faces of the specimen during SHPB tests at the strain rate of  $10000 \text{ s}^{-1}$ , Figure 6 displays the typical set of waveforms recorded by strain gauges glued onto the pressure bars and the corresponding 1- and 2-wave stress curves under high temperatures at the strain rate of  $10000 \text{ s}^{-1}$ . The 1-wave stress analysis indicates the stress conditions at the specimen-transmitted bar interface. The 2-wave analysis denotes the stress conditions at the incident bar-specimen interface, where the sum of incident wave and reflected waves is proportional to the sample front stress. As can be seen from Figures 6(b) and 6(d), a good agreement between the 1-wave and the 2-wave stress-strain response is reached, which represents the stress-state equilibrium within the

specimen and therefore illustrates the validity of the SHPB test results.

**3.1. Strain Rate Hardening Effect on the Flow Stress.** The dynamic compressive flow response under varying indicated temperatures is presented in Figure 7. Although deformed, none of the tested samples brought about fracture. Thus, the ending parts of the stress-strain curves indicate unloading instead of fracture. The influence of strain rate on the flow response of U71Mn as a function of temperature at  $\varepsilon = 0.1$  is displayed in Figure 8. The impact of strain rates on flow stress at other strain values is also similar. From Figure 7, it is found that the plastic flow stress of the samples hinges upon strain rate and presents the strain rate hardening effect, which means that the flow stress increases as strain rate increases. The strain rate hardening effect is caused by dislocation pileup, since dislocation density is increased when the strain rate increases, and thus hardening occurs. Nevertheless, the impact of strain rates on the flow response is weakened as temperature increases. When the specimens were dynamically compressed at  $800^\circ\text{C}$ , as shown in Figure 7(e), all of the stress-strain curves under varied strain rates show tardily progressive tendency before unloading and the true stresses are quite low. The reason is that the tested specimens are softened severely at  $800^\circ\text{C}$  so that the flow stress is relatively low, which means that the specimens are easier to deform plastically.

According to [27], strain rate dependence on the plastic flow stress can be determined quantitatively by introducing a strain rate sensitivity parameter  $\beta$ , and this parameter is expressed as

$$\beta = \frac{\sigma_2 - \sigma_1}{\ln(\dot{\varepsilon}_2/\dot{\varepsilon}_1)}, \quad (2)$$

where  $\sigma_1$  and  $\sigma_2$  are the experimentally obtained flow stresses at strain rates of  $\dot{\varepsilon}_1$  and  $\dot{\varepsilon}_2$  under a given plastic strain and temperature, respectively.

For U71Mn rail steel, the strain rate sensitivity  $\beta$  as a function of strain at  $1500 \text{ s}^{-1}$ – $10000 \text{ s}^{-1}$  under different temperatures is presented in Figure 9. It can be noticed that  $\beta$  decreases as the temperature rises when the temperature is under  $600^\circ\text{C}$ , particularly from  $20^\circ\text{C}$  to  $200^\circ\text{C}$ , whereas it enhances when the temperature is up to  $800^\circ\text{C}$ , which means that the material still has some certain strain rate strengthening effect at very high temperatures and the effect is not weaker than that at  $600^\circ\text{C}$ , indicating that the material still shows some certain strain rate strengthening effect. It can be also observed from Figure 9 that  $\beta$  decreases rapidly as strain increases under  $20^\circ\text{C}$ ,  $400^\circ\text{C}$ , and  $600^\circ\text{C}$ , while it remains nearly invariable with regard to strain under  $200^\circ\text{C}$  and  $800^\circ\text{C}$ .

**3.2. Thermal Softening Effect on the Flow Stress.** Figure 10 presents the dynamic flow response at varying indicated strain rates. The impact of temperature on the flow behavior of U71Mn as a function of strain rate at  $\varepsilon = 0.1$  is given in Figure 11. The temperature effect on the flow response under other strains is similar. Figures 10(a)–10(c)

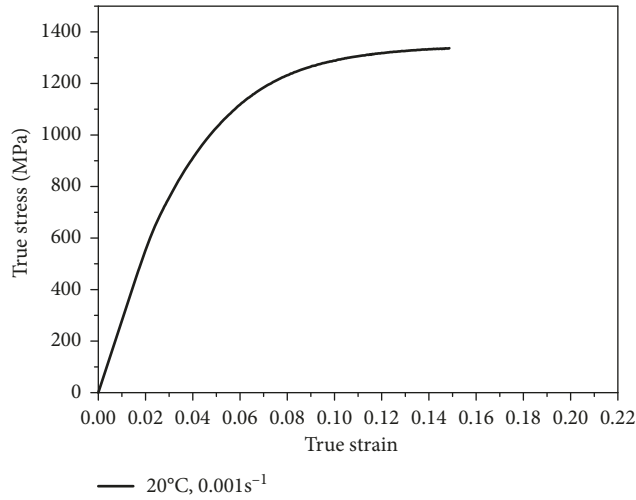
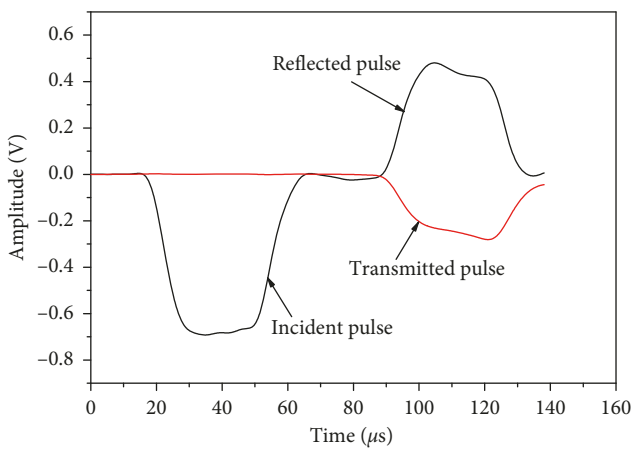
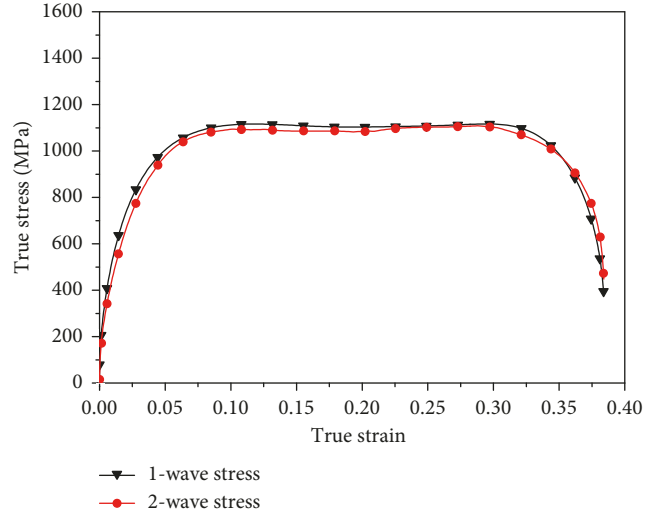


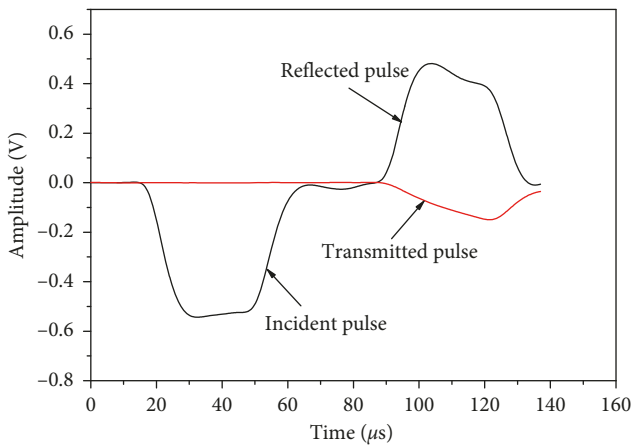
FIGURE 5: True flow strain-stress curve of U71Mn rail steel at  $0.001\text{ s}^{-1}$  and  $20^\circ\text{C}$ .



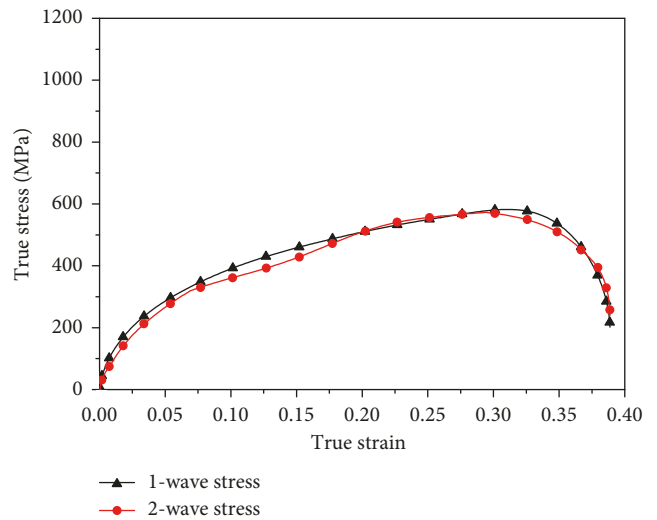
(a)



(b)

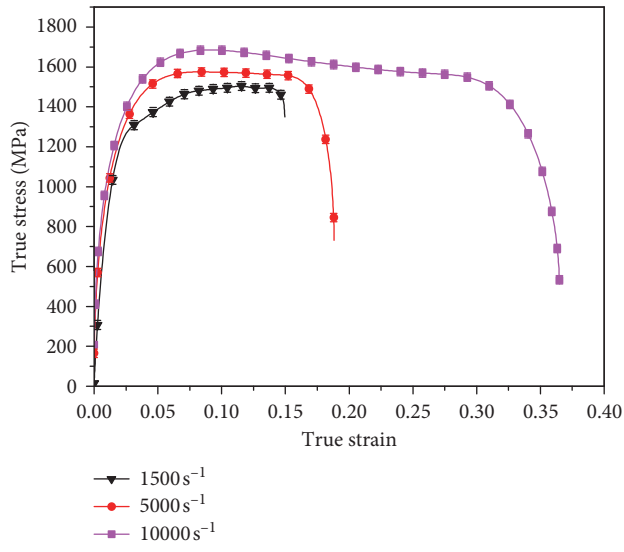


(c)

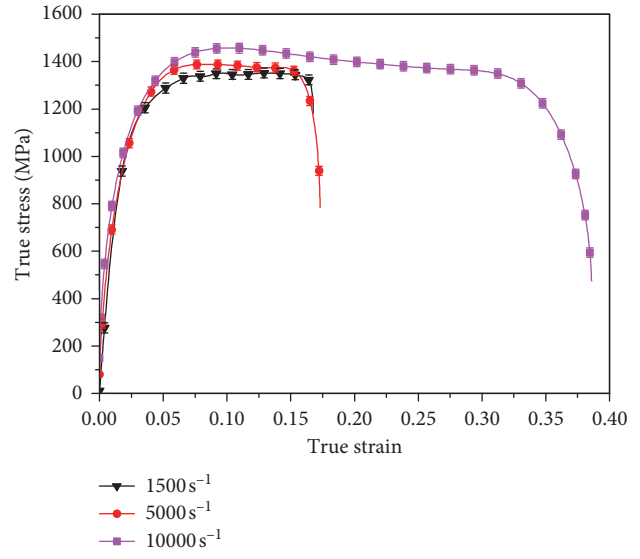


(d)

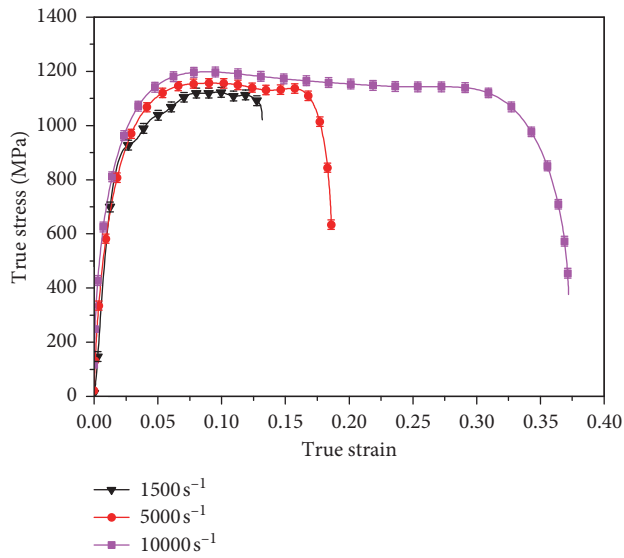
FIGURE 6: Typical strain gauge signals and the corresponding 1- and 2-wave stress curves obtained during the SHPB test with U71Mn samples: (a) strain gauge signals at  $10000\text{ s}^{-1}$  and  $600^\circ\text{C}$ ; (b) 1- and 2-wave stress curves at  $10000\text{ s}^{-1}$  and  $600^\circ\text{C}$ ; (c) strain gauge signals at  $10000\text{ s}^{-1}$  and  $800^\circ\text{C}$ ; (d) 1- and 2-wave stress curves at  $10000\text{ s}^{-1}$  and  $800^\circ\text{C}$ .



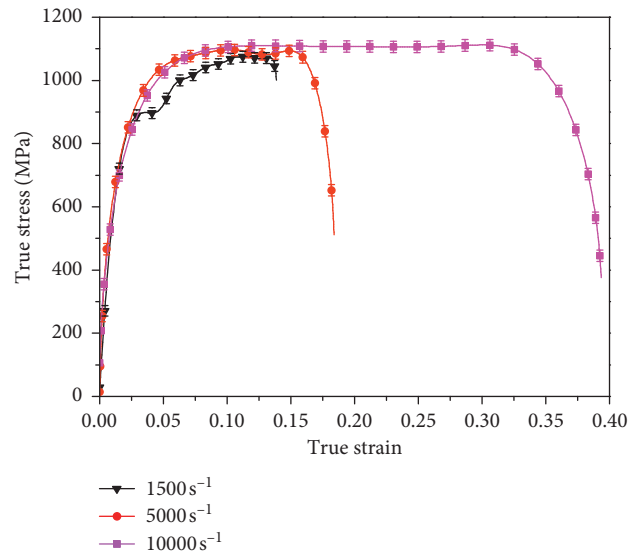
(a)



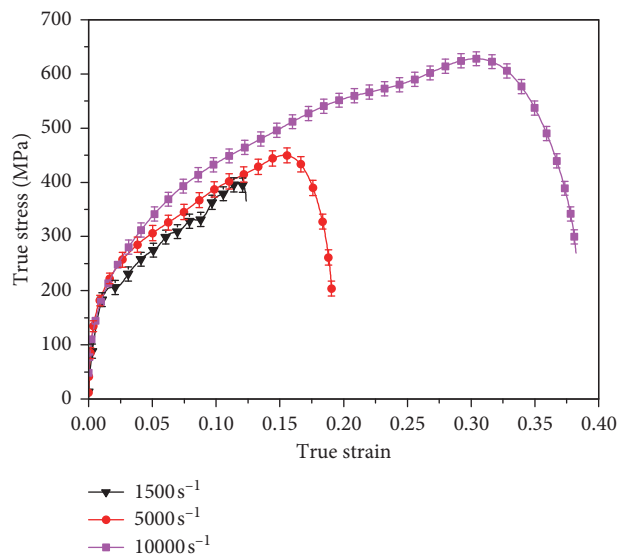
(b)



(c)



(d)



(e)

FIGURE 7: Flow stress-strain curves of U71Mn rail steel in SHPB tests under varying prescribed temperatures: (a) 20°C; (b) 200°C; (c) 400°C; (d) 600°C; (e) 800°C.

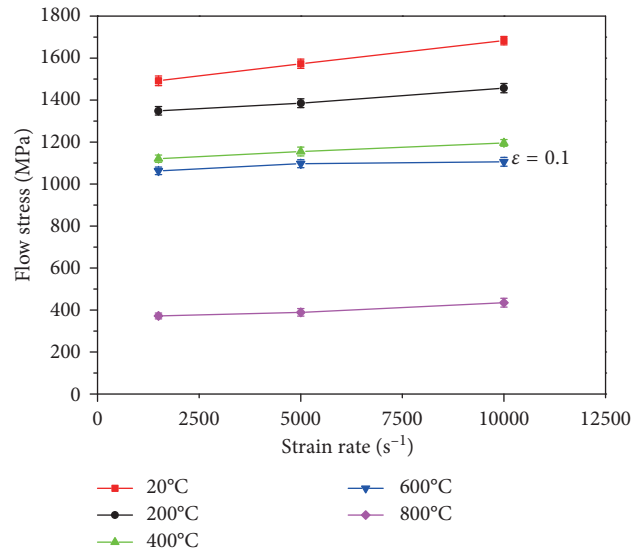


FIGURE 8: Effect of strain rate on the flow stress of U71Mn rail steel at  $\varepsilon = 0.1$ , as a function of temperature.

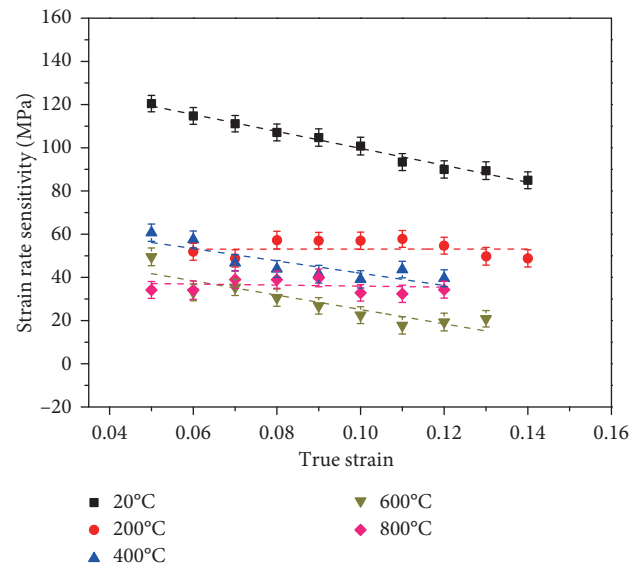


FIGURE 9: Strain rate sensitivity at  $1500 \text{ s}^{-1}$ – $10000 \text{ s}^{-1}$  under varying temperatures.

show that the temperature impact on the flow response of the studied material is far more pronounced than that of the strain rate; i.e., U71Mn rail steel shows strong thermal softening effect. The flow stress reduces rapidly as the temperature rises under varying prescribed strain rates at a constant strain. There is no much difference in flow stress when the temperatures are 400°C and 600°C, respectively, which means that the flow response is insensitive to temperatures at this temperature range. However, the flow stress decreases more evidently as the temperature rises from 600°C to 800°C, which indicates the enhanced temperature sensitivity of the material within this temperature range.

According to [21], temperature dependence on flow stress can be quantitatively evaluated by introducing a temperature sensitivity parameter  $n_a$ , which is expressed as

$$n_a = -\frac{\ln(\sigma_2/\sigma_1)}{\ln(T_2/T_1)} \quad (3)$$

where  $\sigma_1$  and  $\sigma_2$  are the flow stresses acquired from tests performed at temperatures of  $T_1$  and  $T_2$ , respectively;  $T_1$  is the reference temperature (taken as 20°C), and  $T_2$  ( $T_2 > T_1$ ) is the experimental temperature.

For U71Mn rail steel, Figure 12 shows the temperature sensitivity  $n_a$  as a function of true strain at  $5000 \text{ s}^{-1}$  under

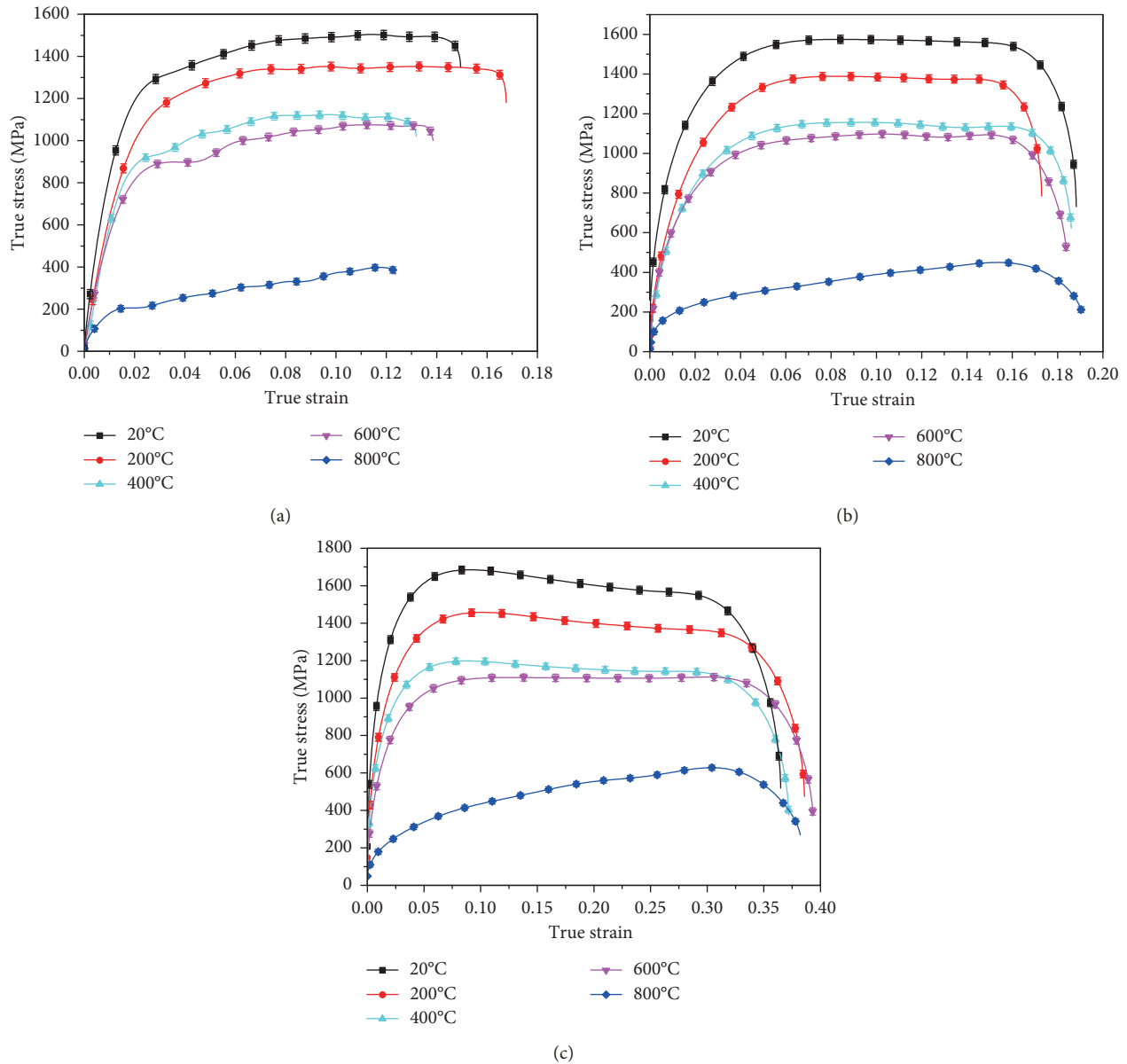


FIGURE 10: Flow stress-strain curves of U71Mn steel in SHPB tests under different strain rates: (a) 1500 s<sup>-1</sup>; (b) 5000 s<sup>-1</sup>; (c) 10000 s<sup>-1</sup>.

varying temperature ranges. It shows that the  $n_a$  increases as temperature rises. A significant observation is that the  $n_a$  undergoes a drastic increment when the temperature is 800°C and there is not much difference in the temperature sensitivity when the temperatures are 400°C and 600°C, respectively. As per Figure 12, the temperature sensitivity slightly decreases with the increase of strain except that there is a more remarkable decrease of the temperature sensitivity with the rise of strain at 800°C.

**3.3. Strain Hardening Effect on the Flow Stress.** The strain hardening rate hinges upon the competition among the impacts of strain rate and strain hardening, together with thermal softening. In Figure 5, it displays that the strain hardening rate is evident under quasistatic compressive

condition, which can be explicated by the fact that the deformation-generated heat at 0.001 s<sup>-1</sup> can dissipate into surroundings quickly so that the thermal softening effect can be ignored. For dynamic tests conducted under dynamic loading conditions, the heat caused by plastic deformation usually occurs in few milliseconds so that it is very hard for the heat to disperse into the ambient environment because of the very short time, which will eventually bring about the temperature increment of the specimen. The large adiabatic heat can reduce the strength of the tested sample, bringing about the reduction of strain hardening rate. Therefore, temperature softening effect serves as a striking part in the specimen deformation under large strain rates, which causes the insensitivity of the flow stress to strains. The high adiabatic temperature rise generated within the specimen during plastic deformation

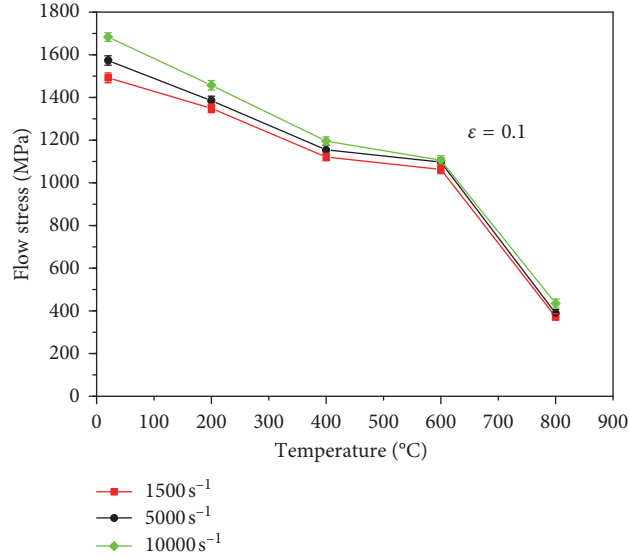


FIGURE 11: Effect of temperature on the flow stress of U71Mn steel at a true strain of 0.1, as a function of strain rate.

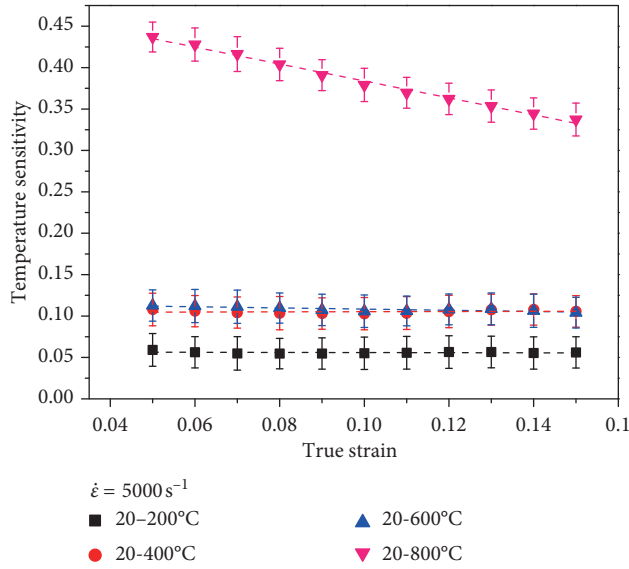


FIGURE 12: Temperature sensitivity at  $5000 \text{ s}^{-1}$  under various temperature ranges.

needs to be taken into account because adiabatic temperature rise can cause the weakening of the strain hardening rate. The temperature increment value is normally calculated by [28]

$$\Delta T = \frac{\zeta}{\rho_s C_v} \int_0^\varepsilon \sigma d\varepsilon, \quad (4)$$

where  $\rho_s$  is the density of the studied material (adopted as  $7.8 \text{ g/cm}^3$ ),  $C_v$  represents the heat capacity (i.e.,  $0.5 \text{ J/g}^\circ\text{C}$ ), and  $\varepsilon$  and  $\sigma$  denote the plastic strain and flow stress, respectively.  $\zeta$  is the Taylor–Quinney coefficient, which means the proportion of the plastic deformation induced heat. In this study,  $\zeta$  is taken as approximately 1.0 for the dynamic loading cases [28]. The integral part in equation (4) signifies the plastic work, namely, the area beneath the stress-strain curve.

Table 3 lists the temperature increment values induced within the deformed specimens under dynamic compressive conditions. It can be seen from Table 3 that adiabatic temperature increment decreases as the experimental temperature rises and that adiabatic temperature increment increases with the increase of strain and strain rate. Therefore, the flow softening phenomenon of U71Mn rail steel at  $20^\circ\text{C}$ – $600^\circ\text{C}$  and strain rates of  $5000 \text{ s}^{-1}$  and  $10000 \text{ s}^{-1}$  in Figures 7(a)–7(d) is probably induced by the temperature softening effect that overshadows that of strain rate and strain. However, the corresponding flow response in Figure 7(e) displays continuous progressive tendency at  $800^\circ\text{C}$ , which implies that the flow response of U71Mn rail steel is dominated by the impacts of the strain rate and strain. In the process of plastic deformation, the slope of the curves in Figure 7 is dominated by the combination result of

TABLE 3: Variation of adiabatic temperature increment under various compressive conditions.

| Temperature (°C) | Strain rate (s <sup>-1</sup> ) | Temperature increment $\Delta T$ (°C) |                  |                   |                  |                   |
|------------------|--------------------------------|---------------------------------------|------------------|-------------------|------------------|-------------------|
|                  |                                | $\epsilon = 0.05$                     | $\epsilon = 0.1$ | $\epsilon = 0.15$ | $\epsilon = 0.2$ | $\epsilon = 0.25$ |
| 20               | 1500                           | 14.02                                 | 32.74            | 51.66             | —                | —                 |
|                  | 5000                           | 15.59                                 | 35.68            | 55.76             | —                | —                 |
|                  | 10000                          | 16.47                                 | 37.86            | 59.22             | 80.02            | 100.36            |
| 200              | 1500                           | 12.11                                 | 29.18            | 46.46             | —                | —                 |
|                  | 5000                           | 12.60                                 | 30.28            | 47.94             | —                | —                 |
|                  | 10000                          | 13.31                                 | 31.63            | 50.20             | 68.33            | 86.12             |
| 400              | 1500                           | 10.15                                 | 24.23            | —                 | —                | —                 |
|                  | 5000                           | 10.63                                 | 25.33            | 39.96             | —                | —                 |
|                  | 10000                          | 11.58                                 | 26.81            | 41.99             | 56.89            | 71.60             |
| 600              | 1500                           | 9.44                                  | 22.47            | —                 | —                | —                 |
|                  | 5000                           | 10.30                                 | 24.12            | 39.09             | —                | —                 |
|                  | 10000                          | 9.89                                  | 23.72            | 37.94             | 52.14            | 66.33             |
| 800              | 1500                           | 2.66                                  | 6.74             | —                 | —                | —                 |
|                  | 5000                           | 3.03                                  | 7.48             | 12.85             | —                | —                 |
|                  | 10000                          | 3.12                                  | 8.15             | 14.14             | 20.92            | 28.22             |

the competition process between the strain hardening effect and the temperature softening effect.

**3.4. Establishment of the Johnson–Cook Model.** As an empirically-based model, the JC model takes into account the effects of strain rate and strain along with temperature on the plastic flow response. These three total effects on the plastic deformation of materials are considered by incorporating them into the model as a multiplicative form. The JC model is written as

$$\sigma = (A + B\epsilon^n)(1 + C \ln \dot{\epsilon}^*)(1 - T^{*m}), \quad (5)$$

where  $\epsilon$  represents the plastic strain,  $\sigma$  denotes the Von Mises flow stress,  $\dot{\epsilon}^* = \dot{\epsilon}/\dot{\epsilon}_0$  represents the dimensionless strain rate ( $\dot{\epsilon}$  means the true strain rate, while  $\dot{\epsilon}_0$  denotes the reference strain rate, i.e., 0.001 s<sup>-1</sup> in the study),  $A$  is the yield stress in MPa under the reference strain rate and temperature,  $B$  means the strain hardening coefficient (MPa),  $C$  is the strain rate hardening coefficient,  $m$  denotes the thermal softening exponent,  $n$  means the strain hardening exponent, and  $T^* = (T - T_r)/(T_m - T_r)$  represents the homologous temperature where  $T_m$  denotes the melting point (taken as 1469°C for the studied steel) and  $T_r$  denotes the reference temperature (taken as 20°C,  $T \geq T_r$ ).

The adiabatic temperature rise  $\Delta T$  induced by dynamic loading exerts a profound influence on the constitutive behavior of the studied material because of the thermal softening effect. Therefore, the conventional JC model needs modifying to involve the temperature softening phenomenon, which is realized by incorporating equation (4) into the temperature term of the original JC model. The temperature term  $T^*$  in equation (5) is transformed to

$$T^* = \frac{T + (\zeta/\rho_s C_v) \int_0^\epsilon \sigma d\epsilon - T_r}{T_m - T_r}. \quad (6)$$

On the basis of the experimentally obtained stress-strain curves given in Figures 5 and 10, the material constants in the original JC model are calculated by regression analysis

technique as the preconditioning values. The value of  $A$  (namely, the stress under the strain of 0.002) at 20°C and 0.001 s<sup>-1</sup> is calculated as 1262 MPa from Figure 5.

The strain rate and temperature impacts are ignored during the uniaxial quasistatic compressive condition. Under 20°C and 0.001 s<sup>-1</sup>, equation (5) will reduce to

$$\sigma = A + B\epsilon^n. \quad (7)$$

Taking the logarithmic transformation on the both sides of equation (7), then equation (7) will transform to

$$\ln(\sigma - A) = \ln B + n \ln \epsilon. \quad (8)$$

Based on the results of quasistatic experiment from Figure 5, the curve of  $\ln(\sigma - A)$  vs.  $\ln \epsilon$  can be plotted by the substitution of  $A$  into equation (8) and by utilizing the values of the stress-strain curve under varying strains from the hardening part of the stress-strain curve.  $B$  can be derived from the intercept of the plot, and meanwhile,  $n$  can be acquired from the slope of the plot.

At 20°C, there is no temperature term. Therefore, equation (5) changes to

$$\sigma = (A + B\epsilon^n)(1 + C \ln \dot{\epsilon}^*). \quad (9)$$

Employing the results of stress-strain curves under a constant strain under 1500 s<sup>-1</sup>, 5000 s<sup>-1</sup>, and 10000 s<sup>-1</sup> from the dynamic compressive tests, the value of  $C$  is derived from the slope of  $[\sigma/(A + B\epsilon^n) - 1]$  vs.  $\ln \dot{\epsilon}^*$  plot.

At 0.001 s<sup>-1</sup>, equation (5) can be transformed as

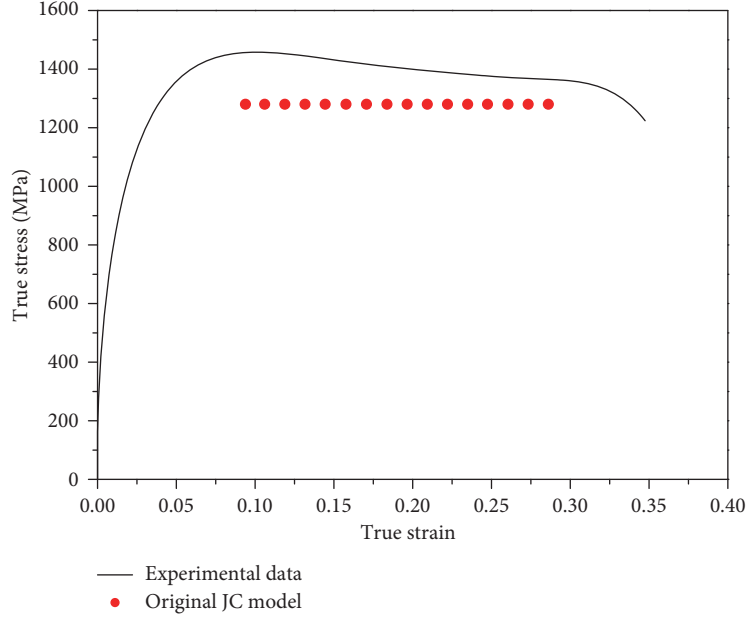
$$\frac{\sigma}{(A + B\epsilon^n)(1 + C \ln \dot{\epsilon}^*)} = 1 - T^{*m}. \quad (10)$$

Using the flow stress values under a fixed strain at varying temperatures (200°C, 400°C, 600°C, and 800°C) and the strain rate of 5000 s<sup>-1</sup>, the value of  $m$  is acquired from the slope of  $\ln\{1 - \sigma/[(A + B\epsilon^n)(1 + C \ln \dot{\epsilon}^*)]\}$  vs.  $\ln T^*$  plot.

Based on the initial fitting results obtained from the preconditioning method above, the least square method is further employed to acquire the final material constants. Table 4 lists the original JC model parameters. Therefore, the

TABLE 4: Material constants in the original JC model for U71Mn.

| Parameter | A (MPa) | B (MPa) | $n$   | C       | $m$     |
|-----------|---------|---------|-------|---------|---------|
| Values    | 1231.54 | 2501.96 | 1.557 | 0.01284 | 0.85624 |

FIGURE 13: Comparison between the experimental and predicted stress using the original JC model at 200°C and 10000 s<sup>-1</sup>.

expression of the JC constitutive equation of U71Mn rail steel is given as follows:

$$\sigma = (1231.54 + 2501.96\epsilon^{1.557}) \left[ 1 + 0.01284 \ln\left(\frac{\dot{\epsilon}}{0.001}\right) \right] \cdot \left[ 1 - \left(\frac{T-20}{1449}\right)^{0.85624} \right]. \quad (11)$$

Figure 13 presents the comparison result between the measured and predicted stress derived from the JC model in its original form at 200°C and 10000 s<sup>-1</sup>. Obviously, appreciable deviation between the experimental and predicted values is observed. Thus, it is a necessity to modify the original JC model. Considering the impact of temperature on the flow response of the studied material, the temperature term in the original JC constitutive model is modified as follows:

$$\sigma = (A + B\epsilon^n)(1 + C \ln \dot{\epsilon}^*)(1 - m_0 T^{*m})(aT + b), \quad (12)$$

where  $a$ ,  $b$ , and  $m_0$  are the constants which describe the relationship between temperature and flow stress. The modified constitutive model of U71Mn rail steel can be acquired as follows:

$$\sigma = (1231.54 + 2501.96\epsilon^{1.557}) \left[ 1 + 0.01284 \ln\left(\frac{\dot{\epsilon}}{0.001}\right) \right] \cdot \left[ 1 - 1.27 \left(\frac{T-20}{1449}\right)^{0.85624} \right] (-0.48T + 361.8). \quad (13)$$

The comparison results between the measured and predicted flow stress employing the modified JC model are presented in Figure 14. Aiming at assessing the predictability of the original and modified JC models, two standard statistical indexes, i.e., correlation coefficient ( $R$ ) and average absolute relative error (AARE), are employed. These two statistical parameters are defined as

$$R = \frac{\sum_{i=1}^{i=N} (\sigma_{\text{exp}}^i - \bar{\sigma}_{\text{exp}})(\sigma_{\text{p}}^i - \bar{\sigma}_{\text{p}})}{\sqrt{\sum_{i=1}^{i=N} (\sigma_{\text{exp}}^i - \bar{\sigma}_{\text{exp}})^2 \sum_{i=1}^{i=N} (\sigma_{\text{p}}^i - \bar{\sigma}_{\text{p}})^2}}, \quad (14)$$

$$\text{AARE}(\%) = \frac{1}{N} \sum_{i=1}^{i=N} \left| \frac{\sigma_{\text{exp}}^i - \sigma_{\text{p}}^i}{\sigma_{\text{exp}}^i} \right| \times 100,$$

where  $\sigma_{\text{exp}}$  is the experimentally-obtained flow stress,  $\sigma_{\text{p}}$  represents the predicted flow stress,  $\bar{\sigma}_{\text{exp}}$  denotes the mean values of  $\sigma_{\text{exp}}$ , and  $\bar{\sigma}_{\text{p}}$  means the mean values of  $\sigma_{\text{p}}$ .  $N$  means the amount of data points. The correlation coefficient  $R$  represents the precision and degree of linear relationship between the measured and estimated data. As an unbiased statistical index, AARE can be employed to evaluate the predictability of a numerical model or equation. Figure 15 presents the correlation between the predicted and measured stress data using the original and modified JC models. In Figures 15(a) and 15(b), the correlation coefficients for the original and modified JC models are 0.84 and 0.98, respectively. The corresponding average absolute relative errors are 21.1% and 8.9%, respectively. By contrast, it can be corroborated that the predictability of the modified JC model is much better than the original one, which indicates

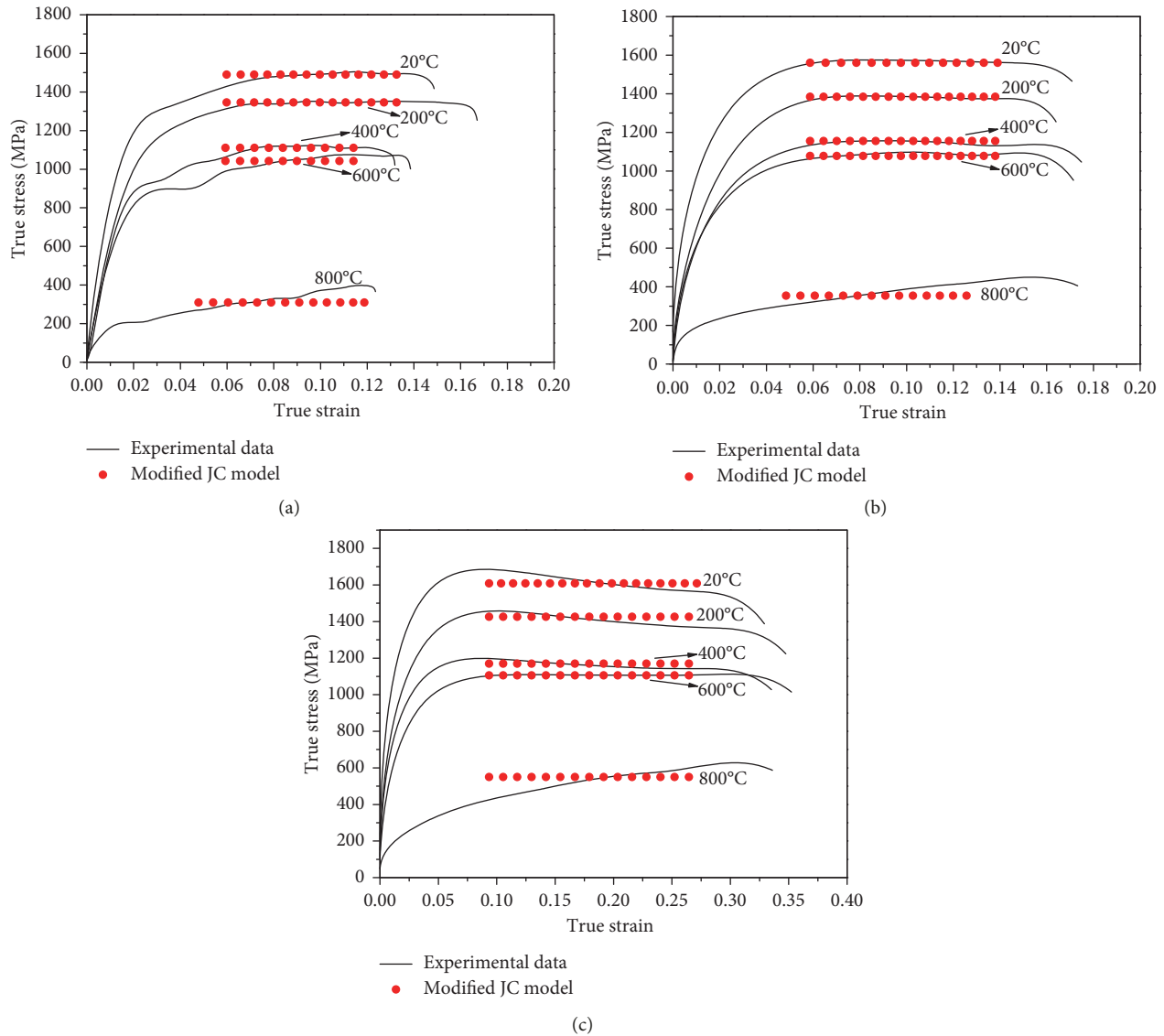


FIGURE 14: Comparison between the experimental and predicted stress using the modified JC model predictions: (a)  $1500 \text{ s}^{-1}$ ; (b)  $5000 \text{ s}^{-1}$ ; (c)  $10000 \text{ s}^{-1}$ .

that equation (13) can be utilized to express the mechanical behavior of U71Mn rail steel.

#### 4. Conclusions

In this paper, the true stress-strain data of U71Mn rail steel have been obtained from the uniaxial compressive experiments performed at a wide range of strain rates ( $0.001\text{--}10000 \text{ s}^{-1}$ ) and temperatures ( $20^\circ\text{C}\text{--}800^\circ\text{C}$ ). The dynamic response of U71Mn rail steel has been investigated by means of the aforementioned experimental results. The following conclusions can be drawn based on the study:

- (1) The strain rate sensitivity of U71Mn decreases with the increase of temperature. Nevertheless, the strain rate sensitivity increases when the temperature is  $800^\circ\text{C}$ . Besides, the strain also has a remarkable

impact on the strain rate sensitivity of the studied material.

- (2) U71Mn rail steel displays remarkable temperature sensitivity. The influence of temperature on the flow behavior is evident with respect to the increasing experimental temperature. However, the temperature effect of the studied material is not conspicuous when the temperatures are  $400^\circ\text{C}$  and  $600^\circ\text{C}$ , respectively. The temperature effect on the flow response is more remarkable than that of strain rate.
- (3) The strain hardening effect of the studied material slightly decreases at temperatures from  $20^\circ\text{C}$  to  $600^\circ\text{C}$  and strain rates of  $5000 \text{ s}^{-1}$  and  $10000 \text{ s}^{-1}$ . However, when the temperature is  $800^\circ\text{C}$ , the strain hardening effect is obvious.
- (4) On the basis of the experimental results, the modified JC model of U71Mn was established by taking into

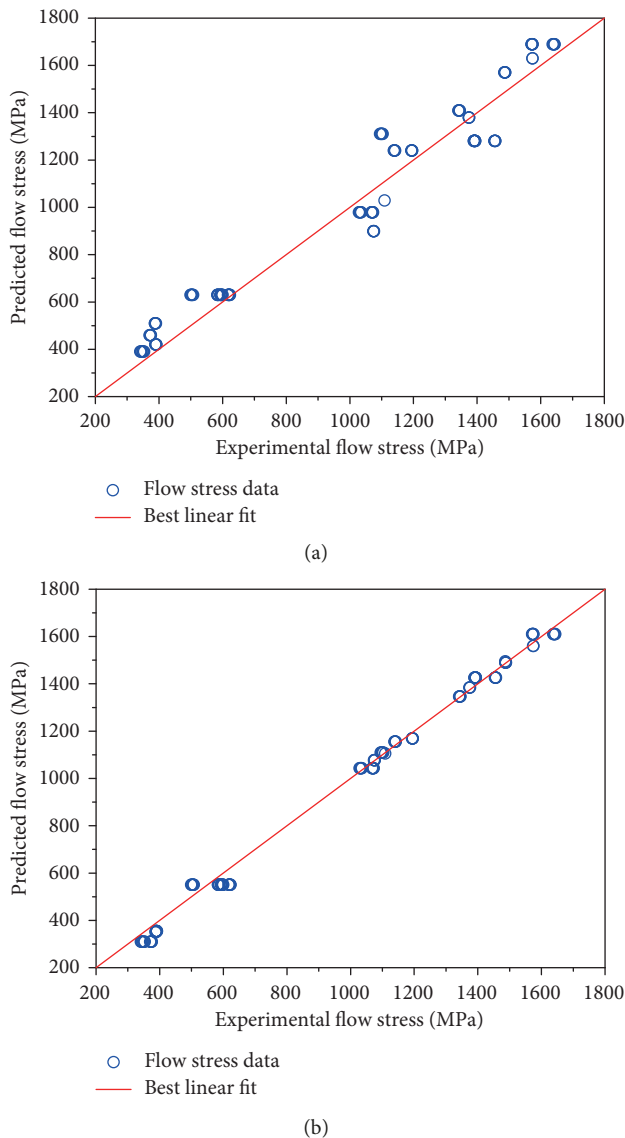


FIGURE 15: Correlation between the measured and predicted flow stresses under varying deformation conditions. (a) Original JC model; (b) modified JC model.

account the effects of high temperature and high strain rate. Compared with the experimental data, the correlation coefficient ( $R$ ) and average absolute relative error (AARE) of the modified JC model are 0.98 and 8.9%, respectively, which shows that the proposed JC model can better express the dynamic mechanical behavior of U71Mn rail steel.

## Data Availability

The data used to support the findings of this study are available from the corresponding author upon request.

## Conflicts of Interest

The authors declare no conflicts of interest.

## Acknowledgments

The authors gratefully acknowledge the National Natural Science Foundation of China (Grant no. 51675184) and the Provincial Science and Technology Project of Guangdong Province (Grant no. 2016A010102006).

## References

- [1] P. T. Torstensson and J. C. O. Nielsen, "Monitoring of rail corrugation growth due to irregular wear on a railway metro curve," *Wear*, vol. 267, no. 1, pp. 556–561, 2009.
- [2] S. Kaewunruen, M. Ishida, and S. Marich, "Dynamic wheel-rail interaction over rail squat defects," *Acoustics Australia*, vol. 43, no. 1, pp. 97–107, 2015.
- [3] D. F. Cannon, K.-O. Edell, S. L. Grassie, and K. Sawley, "Rail defects: an overview," *Fatigue*, vol. 26, no. 10, pp. 865–886, 2003.
- [4] S. Maya-Johnson, A. J. Ramirez, and A. Toro, "Fatigue crack growth rate of two pearlitic rail steels," *Engineering Fracture Mechanics*, vol. 138, pp. 63–72, 2015.
- [5] S. L. Grassie, "Rail corrugation: advances in measurement, understanding and treatment," *Wear*, vol. 258, no. 7–8, pp. 1224–1234, 2005.
- [6] W. Zhong, J. J. Hu, Z. B. Li, Q. Y. Liu, and Z. R. Zhou, "A study of rolling contact fatigue crack growth in U75V and U71Mn rails," *Wear*, vol. 271, no. 1–2, pp. 388–392, 2011.
- [7] M. Steenbergen and R. Dollevoet, "On the mechanism of squat formation on train rails—Part I: origination," *International Journal of Fatigue*, vol. 47, pp. 361–372, 2013.
- [8] M. Steenbergen, "Rolling contact fatigue in relation to rail grinding," *Wear*, vol. 356–357, pp. 110–121, 2016.
- [9] S. Seo, O. Min, and H. Yang, "Constitutive equation for Ti–6Al–4V at high temperatures measured using the SHPB technique," *International Journal of Impact Engineering*, vol. 31, no. 6, pp. 735–754, 2005.
- [10] G. I. Mylonas and G. N. Labeas, "Mechanical characterisation of aluminium alloy 7449-T7651 at high strain rates and elevated temperatures using split Hopkinson bar testing," *Experimental Techniques*, vol. 38, no. 2, pp. 26–34, 2014.
- [11] G. R. Johnson and W. H. Cook, "A constitutive model and data for metals subjected to large strains, high strain rates and high temperatures," in *Proceedings of the 7th International Symposium on Ballistics*, pp. 541–547, Hague, Netherlands, April 1983.
- [12] F. J. Zerilli and R. W. Armstrong, "Dislocation-mechanics-based constitutive relations for material dynamics calculations," *Journal of Applied Physics*, vol. 61, no. 5, pp. 1816–1825, 1987.
- [13] P. S. Follansbee and U. F. Kocks, "A constitutive description of the deformation of copper based on the use of the mechanical threshold stress as an internal state variable," *Acta Metallurgica*, vol. 36, no. 1, pp. 81–93, 1988.
- [14] Y. Karpat, "Temperature dependent flow softening of titanium alloy Ti6Al4V: an investigation using finite element simulation of machining," *Journal of Materials Processing Technology*, vol. 211, no. 4, pp. 737–749, 2011.
- [15] L. Gambirasio and E. Rizzi, "An enhanced Johnson–Cook strength model for splitting strain rate and temperature effects on lower yield stress and plastic flow," *Computational Materials Science*, vol. 113, pp. 231–265, 2016.
- [16] X. Wang, C. Huang, B. Zou, H. Liu, H. Zhu, and J. Wang, "Dynamic behavior and a modified Johnson–Cook constitutive model of Inconel 718 at high strain rate and elevated temperature," *Materials Science and Engineering: A*, vol. 580, no. 37, pp. 385–390, 2013.

- [17] Y. Zhao, J. Sun, J. Li, Y. Yan, and P. Wang, "A comparative study on Johnson-Cook and modified Johnson-Cook constitutive material model to predict the dynamic behavior laser additive manufacturing FeCr alloy," *Journal of Alloys and Compounds*, vol. 723, 2017.
- [18] M. Hokka, T. Leemet, A. Shrot, M. Baeker, and V. T. Kuokkala, "Characterization and numerical modeling of high strain rate mechanical behavior of Ti-15-3 alloy for machining simulations," *Materials Science and Engineering: A*, vol. 550, no. 6, pp. 350–357, 2012.
- [19] F. Abed, A. Abdul-Latif, and A. Yehia, "Experimental study on the mechanical behavior of EN08 steel at different temperatures and strain rates," *Metals*, vol. 8, no. 9, p. 736, 2018.
- [20] W. S. Lee and C. F. Lin, "High-temperature deformation behaviour of Ti6Al4V alloy evaluated by high strain-rate compression tests," *Journal of Materials Processing Technology*, vol. 75, no. 1-3, pp. 127–136, 1998.
- [21] W. S. Lee, C. F. Lin, and T. J. Liu, "Impact and fracture response of sintered 316L stainless steel subjected to high strain rate loading," *Materials Characterization*, vol. 58, no. 4, pp. 363–370, 2007.
- [22] R. Nakkalil, J. R. H. Jr, and M. N. Bassim, "Characterization of the compression properties of rail steels at high temperatures and strain rates," *Materials Science and Engineering: A*, vol. 141, no. 2, pp. 247–260, 1991.
- [23] L. Jing, L. Han, L. Zhao, and Y. Zhang, "The dynamic tensile behavior of railway wheel steel at high strain rates," *Journal of Materials Engineering and Performance*, vol. 25, no. 11, pp. 4959–4966, 2016.
- [24] K. K. Gu, Q. Lin, W. J. Wang et al., "Analysis on the effects of rotational speed of grinding stone on removal behavior of rail material," *Wear*, vol. 342-343, no. 3, pp. 52–59, 2015.
- [25] S. Nemat-Nasser, *ASM Handbook: Mechanical Testing and Evaluation*, Vol. 8, ASM International, Materials Park, OH, USA, 2000.
- [26] R. Zwiessler, T. Kenkmann, M. H. Poelchau, S. Nau, and S. Hess, "On the use of a split Hopkinson pressure bar in structural geology: high strain rate deformation of Seeberger sandstone and Carrara marble under uniaxial compression," *Journal of Structural Geology*, vol. 97, pp. 225–236, 2017.
- [27] W. S. Lee and C. F. Lin, "Plastic deformation and fracture behaviour of Ti-6Al-4V alloy loaded with high strain rate under various temperatures," *Materials Science and Engineering: A*, vol. 241, no. 1-2, pp. 48–59, 1998.
- [28] S. Nemat-Nasser, W. G. Guo, and D. P. Kihl, "Thermo-mechanical response of AL-6XN stainless steel over a wide range of strain rates and temperatures," *Journal of the Mechanics and Physics of Solids*, vol. 49, no. 8, pp. 1823–1846, 2001.



**Hindawi**  
Submit your manuscripts at  
[www.hindawi.com](http://www.hindawi.com)

